JGR Space Physics

RESEARCH ARTICLE
10.1029/2025JA033811

Dayside Reconnection and Associated Cusp Structure in Response to Solar Wind Rotational Discontinuity (RD) in ANGIE3D Simulation

Xiaolei Li[1], Xueyi Wang[1], Yu Lin[1], Chih-Ping Wang[2], Simon Wing[3], Gonzalo Cucho-Padin[4,5], and Huayue Chen[1]

[1]Department of Physics, Auburn University, Auburn, AL, USA, [2]University of California Los Angeles, Los Angeles, CA, USA, [3]The Johns Hopkins University Applied Physics Laboratory, Laurel, MD, USA, [4]Space Weather Laboratory, NASA Goddard Space Flight Center, Greenbelt, MD, USA, [5]Department of Physics, Catholic University of America, Washington, DC, USA

Abstract Solar wind directional discontinuities, such as rotational discontinuities (RDs), significantly influence energy and transport processes in the Earth's magnetosphere. A recent observational study identified a long-lasting double cusp precipitation event associated with RD in solar wind on 10 April 2015. To understand the magnetosphere-ionosphere response to the solar wind RD, a global hybrid simulation of the magnetosphere was conducted, with solar wind conditions based on the observation event. The simulation results show significant variations in the magnetopause and cusp regions caused by the passing RD. After the RD propagates to the magnetopause, ion precipitation intensifies, and a double cusp structure at varying latitudes and longitudes forms near noon in the northern hemisphere, which is consistent with the satellite observations by Wing et al. (2023, https://doi.org/10.1029/2023gl103194). Regarding dayside magnetopause reconnection, the simulation reveals that the high-latitude reconnection process persists during the RD passing, regardless of whether the interplanetary magnetic field (IMF) with a high B_y/B_z ratio has a positive or negative B_z component, and low-latitude reconnection occurs after the RD reaches the magnetopause at noon when the IMF turns southward. By examining the ion sources along the magnetic field lines, a connection is found between the single- or double-cusp ion precipitation and the solar wind ions entering from both high-latitude and low-latitude reconnection sites. This result suggests that the double-cusp structure can be triggered by magnetic reconnection occurring at both low latitudes and high latitudes in the opposite hemispheres, associated with a large B_y/B_z ratio of the IMF around the RD.

Plain Language Summary A global hybrid simulation was conducted to investigate the dayside solar wind-magnetosphere coupling process driven by the interaction of a rotational discontinuity (RD) with the magnetosphere. RD is a type of discontinuity characterized by a rotation in the magnetic field tangential component and a nonzero, continuous normal component on both sides. In this study, the RD has a prominent eastward magnetic field with a northward (southward) component on the earthward (sunward) side. The simulation results indicate that the dayside magnetopause reconnection sites vary from solely high latitudes to simultaneously high and low latitudes during this RD passing through the dayside magnetopause. This change in reconnection topology leads to a transition in ion precipitation patterns—from a single-cusp to a double-cusp configuration.

Key Points:

- The simulation reveals the evolution of dayside reconnection sites and polar ion precipitation structures in response to the rotational discontinuitie passage
- The simulation identifies high-latitude reconnection sites as a potential new source of cusp ion precipitation in the opposite hemisphere
- Our study demonstrates that 3D global hybrid simulations provide a reliable framework for understanding dayside ion precipitation processes

Supporting Information:

Supporting Information may be found in the online version of this article.

Correspondence to:

X. Li and X. Wang,
lxllxl6109@gmail.com;
wangxue@auburn.edu

Citation:

Li, X., Wang, X., Lin, Y., Wang, C.-P., Wing, S., Cucho-Padin, G., & Chen, H. (2025). Dayside reconnection and associated cusp structure in response to solar wind rotational discontinuity (RD) in ANGIE3D simulation. *Journal of Geophysical Research: Space Physics*, *130*, e2025JA033811. https://doi.org/10.1029/2025JA033811

Received 31 JAN 2025
Accepted 17 AUG 2025

Author Contributions:

Conceptualization: Chih-Ping Wang, Simon Wing
Data curation: Xueyi Wang, Yu Lin, Chih-Ping Wang, Simon Wing
Formal analysis: Xiaolei Li
Funding acquisition: Xueyi Wang, Yu Lin, Chih-Ping Wang, Simon Wing
Investigation: Xiaolei Li
Methodology: Xueyi Wang, Yu Lin
Software: Xueyi Wang, Yu Lin
Supervision: Xueyi Wang
Validation: Xueyi Wang, Yu Lin
Visualization: Xiaolei Li
Writing – original draft: Xiaolei Li
Writing – review & editing: Xueyi Wang, Yu Lin, Chih-Ping Wang, Simon Wing, Gonzalo Cucho-Padin, Huayue Chen

1. Introduction

Large-scale solar wind transients, such as coronal mass ejections and corotating interaction regions, can drive prolonged and intense geomagnetic storms and substorms (e.g., Borovsky & Denton, 2006; Liou et al., 2018; Yermolaev et al., 2012). In contrast, narrower solar wind transients—such as interplanetary shock and magnetohydrodynamic (MHD) discontinuities—tend to induce rapid, short-term impacts on the Earth's magnetosphere (e.g., Andréeová & Přech, 2007; Farrugia et al., 2022; Hsu & McPherrron, 2003; Lukin et al., 2024). The most frequently observed discontinuities in the interplanetary magnetic field (IMF) are directional discontinuities (DDs) (e.g., Burlaga, 1969; Lepping & Behannon, 1986). Across DDs, only the magnetic field direction changes, while the magnetic field strength and plasma density remain constant. Rotational discontinuities (RDs) represent a specific class of DDs characterized by nonzero normal components of both the magnetic field and plasma flow velocity across the discontinuity.

The geomagnetic effects of DDs are closely linked to different IMF directions on either side of the discontinuity, especially when the IMF B_z component reverses sign across the RD. Observational studies have shown that the passage of an RD can trigger magnetic reconnection at the magnetopause (e.g., Lukin et al., 2024). The magnetopause reconnection process can accelerate charged particles, leading them to penetrate through the cusp region—where open magnetic field lines converge toward the magnetic poles (e.g., Newell & Meng, 1994). Energetic particles within the loss cone in the cusp ultimately precipitate into the ionosphere, giving rise to cusp aurora (e.g., Bobra et al., 2004).

In a simplified scenario, a predominantly northward (southward) IMF drives magnetopause reconnection at latitudes poleward (equatorward) of the cusp, resulting in the cusp ion precipitation observed at higher (lower) latitudes in the ionosphere (Frey et al., 2007; Lavraud & Cargill, 2005). Under IMF conditions with a higher B_y/B_z ratio, the reconnection cites may extend toward the dawn and dusk flanks of the high-latitude magnetopause (Crooker, 1979; Trattner et al., 2017). At low latitudes, the reconnection neutral line can become tilted across the subsolar point when IMF $B_z < 0$ (e.g., Cowley & Owen, 1989; Trattner et al., 2007, 2021). Cusp particle precipitation may also shift in magnetic latitude or longitude depending on factors such as the dipole tilt angle, the IMF B_y and B_z components, and solar wind dynamic pressure (e.g., Bobra et al., 2004; Frey et al., 2007; Frey, Phan, et al., 2003, Frey, Mende, et al., 2003; Phan et al., 2003). Under steady IMF conditions with a constant clock angle, observations suggest that the dayside magnetopause reconnection X-line remains quasi-stationary (Fuselier et al., 2019), leading to corresponding steady ion precipitation patterns (e.g., Fuselier et al., 2003; Petrinec & Fuselier, 2003).

The "double cusp" phenomenon refers to the observation of two distinct particle precipitation regions—both identified as polar cusps—counted in quick succession by a single spacecraft. Two primary explanations have been proposed for this feature. One hypothesis suggests that a single cusp region shifts position and intersects the spacecraft trajectory twice due to variations in upstream solar wind conditions (e.g., Escoubet et al., 2013; Zong et al., 2008). The alternative explanation posits the existence of two distinct and steady cusp precipitation regions arising from simultaneous high-latitude and low-latitude magnetic reconnection at the dayside magnetopause (e.g., Wing et al., 2001). Under this scenario, double cusp particles may originate from low-latitude reconnection entry points when the IMF $B_z < 0$, and from high-latitude anti-parallel magnetopause reconnection sites when IMF has a strong B_y component (e.g., Crooker, 1979; Newell et al., 1989, 1995, 2004; Pitout et al., 2009; Wing et al., 1996).

The physical processes underlying the geomagnetic effects of solar wind discontinuities can be investigated using global simulations. Three-dimensional (3D) MHD simulations combined with test-particle tracing techniques have been employed to reproduce the energy dispersion patterns of cusp ions across various latitudes (Connor et al., 2012, 2015). While MHD models provide valuable large-scale insights, hybrid simulations offer a more detailed representation by incorporating ion-scale kinetic effects, enabling a more direct capture of the ion precipitation process. For example, Grandin et al. (2023) employed global 3D hybrid-Vlasov simulations to model dayside cusp proton precipitation associated with magnetopause reconnection, showing good agreement with observations. Unlike the hybrid-Vlasov approach—which includes three additional velocity-space dimensions—the hybrid particle-in-cell (PIC) method represents ion velocity distributions statistically through macroparticles. This allows the hybrid PIC approach to achieve higher spatial resolution at comparable computation cost. Global hybrid PIC simulations have demonstrated the formation and evolution of reconnection at the dayside magnetopause and within the magnetosheath when an RD propagates from the bow shock to the magnetopause (Guo, Lin, & Wang, 2021, Guo, Lin, Wang, & Du, 2021; Lukin et al., 2024; Tan et al., 2011; Wang et al., 2019). Earlier studies also employed global hybrid PIC simulations to examine the relationship between magnetopause reconnection and the energy-dispersed spectrum of cusp-precipitating ions under purely southward IMF conditions (Tan et al., 2012).

Focusing on the short-term (<10 min) effects of DDs on dayside cusp ion precipitation, Wing et al. (2023, 2024) analyzed a solar wind RD event that occurred on 10 April 2015. This RD was characterized by a steady and elevated IMF B_y/B_z ratio on both sides of the discontinuity. Their analysis revealed that the RD induced complex structures in the magnetosphere, from the magnetopause down to the cusp in the ionosphere. Notably, a long-lasting double cusp feature was observed in the northern hemisphere following the RD's arrival. Based on Wing et al. (2001), this feature was attributed to simultaneous magnetic reconnection occurring at both low and high latitudes.

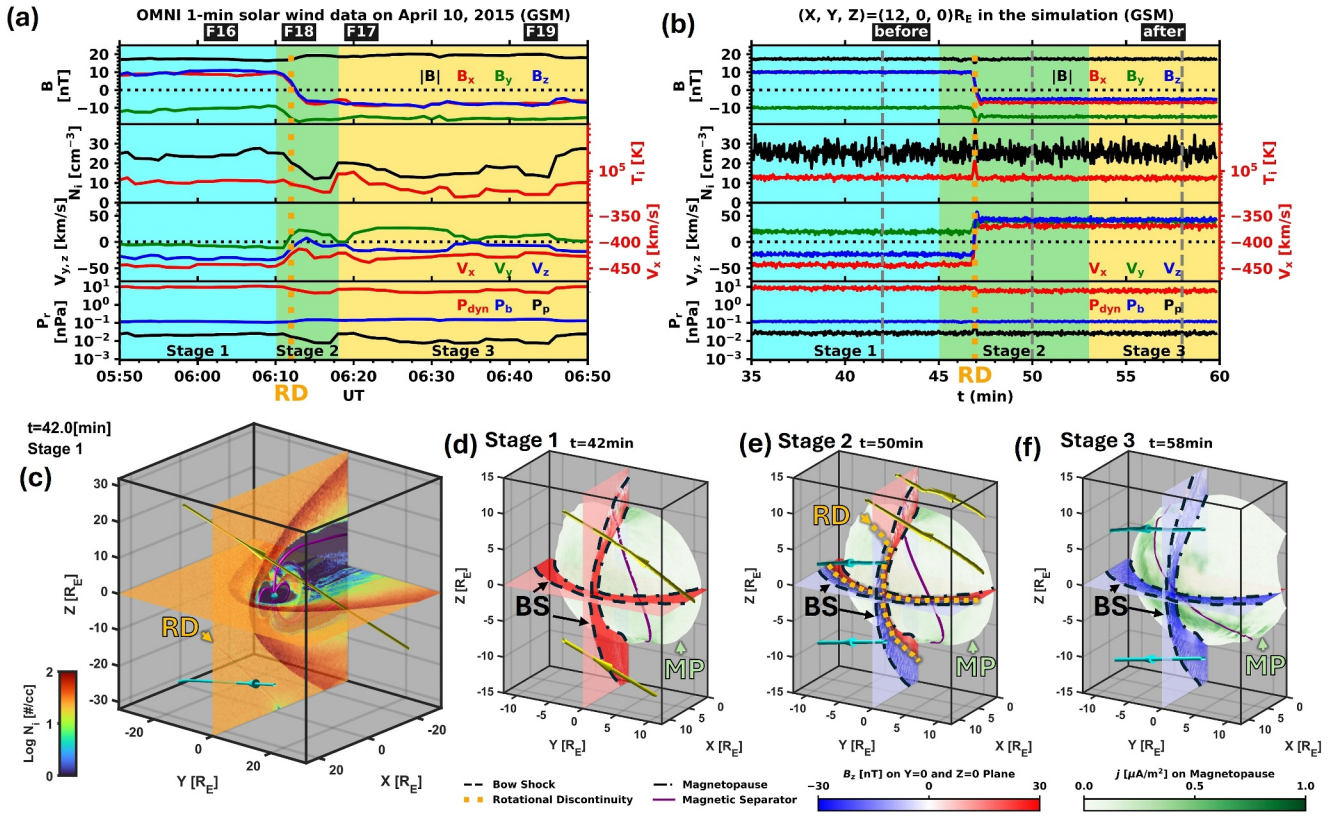

Figure 1. Solar wind conditions and 3D view of the passage of rotational discontinuitie (RD) through Earth's magnetosphere. (a), (b) OMNI 1-min solar wind data and corresponding solar wind conditions at $(X, Y, Z) = (12, 0, 0)$ ahead of the bow shock in the simulation: interplanetary magnetic field magnitude ($|B|$), B_x, B_y, and B_z in the first panel, proton number density (N_i) and temperature (T_i) in the second panel, proton speed V_x, V_y, and V_z in the third panel, solar wind dynamic pressure (P_{dyn}), magnetic pressure (P_b), and proton thermal pressure (P_p) in the fourth panel from top to bottom. Orange vertical dotted line indicates the arrival time of rotational discontinuity (RD). Stages 1–3 are marked as cyan, green and gold. "F16"–"F19" in (a) indicate the observation time of the northern cusp precipitation structure for DMSP F16-F19. "Before" and "after" in b indicate the time for displaying the northern cusp ion precipitation structure in stages 1 and 3. Vertical gray dashed lines in (b) each represent 42, 50, and 58 min in the simulation, corresponding to both (c) and (d), (e), and (f). (c)–(f) The passage of RD in the solar wind through the Earth's magnetosphere occurs at 42 (c) and (d), 50 (e), and 58 (f) minutes, corresponding to stage 1–3 in the simulation. Figure (c) displays the full simulation domain range for (d)–(f) focus on the dayside of the magnetosphere. Open magnetic field lines on both sides of the RD are marked by yellow and cyan 3D tubes with arrows. The color on the planes at $X = 0$ R_E and $Y = 0$ R_E represents N_i or B_z component in (c) or (d)–(f). In (d)–(f), the bow shock (BS) and magnetopause (MP) are delineated on the two planes by thin black dashed and dashed-dotted lines, respectively, while the RD is indicated by thick orange dotted lines. The surface illustrates the 3D position of the MP on the dayside, with color indicating the local electric current strength (j). The purple curve on the MP connecting the regions of high j is the magnetic separator.

To better understand the physical processes that lead to the complex structures at magnetopause and in the cusp region, we performed a 3D global hybrid PIC simulation of the event reported by Wing et al. (2023). In this event, the RD was characterized by a high IMF B_y/B_z ratio and a weak B_z component that rotated from positive to negative across the discontinuity. This paper is organized as follows. Section 2 describes the simulation model and the upstream solar wind conditions. Section 3 presents the simulation results, including the formation and evolution of dayside reconnection during the RD passaging (Section 3.1) and its impact on ion precipitation into the northern hemisphere ionosphere (Section 3.2).

2. Simulation Model and Solar Wind Conditions

In this study, we simulate the RD event reported by Wing et al. (2023) using our global hybrid PIC code, the AuburN Global hybrid CodE in 3D (ANGIE3D) (see Lin et al., 2014 for details). In hybrid simulations, ions and electrons are each treated as discrete particles and massless fluids, respectively. The simulation domain is constructed in Geocentric Solar Magnetospheric (GSM) coordinates with a three-dimensional grid of $(N_x, N_y, N_z) = (841, 768, 768)$, spanning X at $[-30, 25]$ R_E, Y at $[-32, 32]$ R_E, and Z at $[-32, 32]$ R_E, as shown in Figure 1c. The Earth's dipole tilt angle is set to be 0° in this run, which closely approximates the actual tilt angle of approximately −1° during the event. The inner boundary is defined at r = 3 R_E, where uniform Pederson

conductance of 10 S and Hall conductance of 5 S are specified in the ionosphere. A cold ion fluid dominates at r < 6 R_E modeling the inner magnetosphere.

The solar wind conditions prior to the RD were imposed at the upstream boundary located at $X = 25\ R_E$. With the solar wind flowing along the GSM -X direction and interacting self-consistently with the geomagnetic dipole field, the bow shock and the magnetopause gradually form. Following this, the RD is introduced and begins to propagate from the upstream boundary.

The solar wind conditions around the RD (Figure 1b) are set based on the OMNI 1-min solar wind properties around the RD event on 10 April 2015 (Figure 1a). As the upstream solar wind properties remain relatively steady on both sides of the RD (Figure 1a), they are implemented as constant values in the simulation (Figure 1b). The RD is launched at time $t = 0$, positioned outside the domain at GSM coordinates $X = 200\ R_E$, $Z = 0\ R_E$. Its normal direction is (−0.664, 0, 0.748), which is perpendicular to GSM Y axis but oblique to both X and Z axis (indicated by the thick orange dotted lines in Figure 1e). The RD propagates at a velocity of (−400, −24, 20) km/s, resulting in an arrival time of about 45 min at the dayside bow shock in the southern hemisphere. Across the RD, both magnetic field strength B and the ion number density N_p remain constant at17.5 nT and 25 cm^{-3}, respectively (Figures 1b and 1c). The IMF (B_x, B_y, B_z) changes from (10, −10, 10) nT with the clock angle of 45° on the earthward side of the RD to (−7, −15, −5.1) nT with a clock angle of 109° on the sunward side, corresponding to a normal magnetic field component $B_n = 0.8$ nT. Note that, unlike the IMF configuration in the event of Bobra et al. (2004)—where $|B_y| < |B_z|$—the RD in this study features $|B_y| \geq |B_z|$, with a finite B_x component on both sides.

3. Simulation Results

Figures 1c–1f illustrates the 3D evolution of the RD as it propagates through Earth's magnetosphere (see also Movies S1 and S2). The RD can be clearly identified in the solar wind and magnetosheath regions as this discontinuity separates the $+B_z$ and $-B_z$ regions on the $Y = 0$ and Z = 0 planes. The RD evolution can be divided into three stages:

1. Stage 1 ($t < 45$ min): The RD remains upstream of the bow shock in solar wind (Figures 1c and 1d).
2. Stage 2 ($45 \leq t < 53$ min): After intersecting the bow shock, the RD enters and propagates through the dayside magnetosheath (Figure 1e). Due to the obliquity of the RD front, its intersection with the bow shock progresses northward, eventually passing over the northern cusp. At the end of this stage, the RD reaches the dayside magnetopause.
3. Stage 3 ($t \geq 53$ min): Following its interaction with the entire dayside magnetopause, the RD moves into and continues propagating within the nightside magnetosheath (Figure 1f).

In Figures 1d–1f, the dayside magnetopause is shown as the outer separatrix surface (see detailed description in Section 3.1.2) with the magnetopause electric current density (jjj) mapped onto it using a green color scale. During stages 1 and 2 (Figures 1d and 1e), strong current density is found at the dawn or dusk side of the magnetic poles at high latitudes. However, in stage 3 (Figure 1f), the strong-current region extends equatorward toward the magnetopause nose, indicating that low-latitude reconnection occurs only during this stage. Additional evidence for potential reconnection sites is provided by the magnetic separator (illustrated as a purple curve in Figures 1d–1f), which intersects the regions of enhanced current density. This feature in the global view will be discussed in more detail in Section 3.1.2.

3.1. Dayside Reconnection During the Passage of RD

3.1.1. Local View on the Occurrence of Low Latitude Reconnection

To investigate the relationship between the position of RD and the onset of low-latitude magnetopause reconnection during stage 3, we examined two equatorial line segments along the GSM X-direction near noon, positioned near potential reconnection sites. As illustrated in Figure 2a, the segments are located at fixed positions (8 $R_E < x < 12\ R_E$), each referred to as L1 (yellow, at $y = 0\ R_E$) and L2 (lime-green, at $y = -2\ R_E$).

Figure 2b shows the temporal evolution of various physical quantities along the segments L1 between 35 and 60 min, including magnetic field components (B_x, B_y, and B_z), ion number density (N_p), and electric current density components (j_x, j_y and j_z). Similar evolution is found along L2. Both L1 and L2 traverse three distinct regions—the solar wind, magnetosheath, and the magnetosphere—as well as two major boundaries: the bow

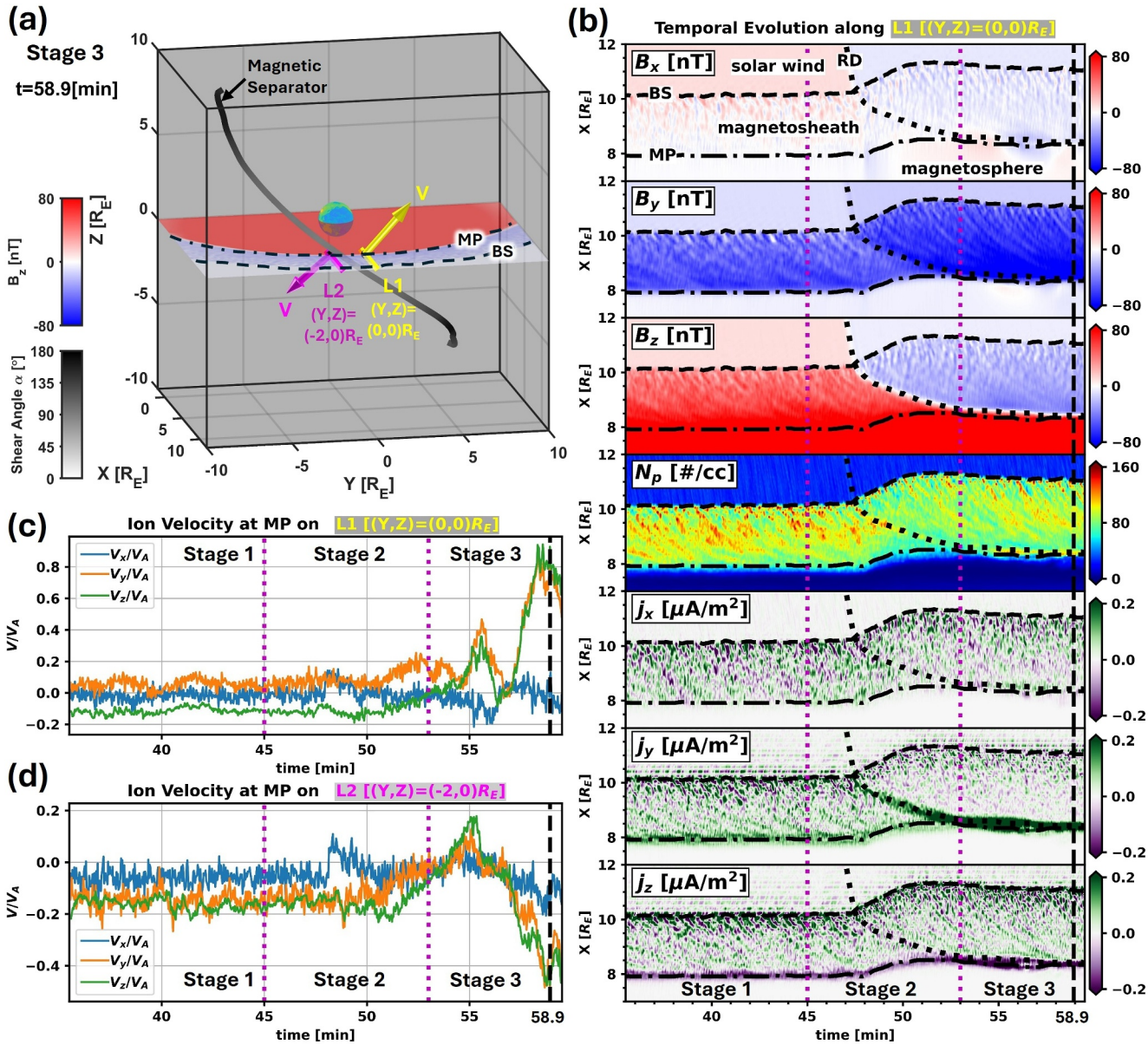

Figure 2. Local evidence of low-latitude reconnection in stage 3. It is based on local properties on two segments, named L1 and L2, at 8 $R_E < x < 12$ R_E, $(y, z) = (0, 0)$ R_E and $(0, -2)$ R_E. (a) Position of L1 (yellow) and L2 (magenta) on the equator plane with color as B_z component at $t = 58.9$ min in stage 3. The yellow/magenta arrow indicates the 3D direction of ion outflow at the intersection of magnetopause and L1/L2. The thick curve is the magnetic separator as potential magnetopause reconnection site with color representing local shear angle. (b) Time variation of magnetic field components (B_x, B_y, B_z), ion number density (N_p), and electric current density components (j_x, j_y, j_z) along L1. The bow shock (BS) and magnetopause (MP) are marked by dashed and dashed-dotted lines in (a) and (d), separating the solar wind, magnetosheath, and magnetosphere. The rotational discontinuitie is marked by a dotted line, meeting the equatorial bow shock at 47 min and merging into the magnetopause after 53 min. (c) Three components of ion velocity normalized by the local Alfvén velocity at the magnetopause position on L1. (d) Same as (c), but for L2. Three stages are separated by purple dotted vertical lines in (b), (c), and (d), while the thick black vertical dashed line marks the time of 58.9 min, corresponding to (a). At this time, the reversal ion outflow velocity rises to a high level on L1 and L2 each above and below the reconnection sites, respectively, as shown in (a), providing local evidence of low-latitude reconnection.

shock (dashed line, labeled BS) and the magnetopause (dashed-dotted line, labeled MP). During stage 2, the standoff distances of BS and MP increase due to the decrease in the solar wind dynamic pressure across the RD from its earthward side to the sunward side. The RD (black dotted line) intersects the equatorial bow shock at $t = 47$ min and slows down in stage 2. It eventually merges with the magnetopause in stage 3. Due to compression by the bow shock and magnetosheath (Guo et al., 2018; Guo, Lin, & Wang, 2021, Guo, Lin, Wang, & Du, 2021), the magnetic shear of the RD is amplified within the magnetosheath—particularly in the δB_z component. This

results in the formation of a strong j_y-dominated current layer around the RD. In stage 3, the RD imposes significant magnetic shear in both the Y- and Z-directions at the magnetopause, as indicated by enhanced current density components j_y and j_z at the equator. This shear-driven current intensification is found to trigger low-latitude magnetopause reconnection during stage 3.

Figures 2c and 2d display the ion velocity components normalized to the local Alfvén velocity (V_A) along the magnetopause intersecting L1 and L2. Since both segments are located near the magnetopause nose, the V_x component remains close to 0. During stages 1 and 2, the magnitudes of V_y and V_z are relatively low, but they increase significantly in stage 3, reaching their peaks of 0.8 V_A (0.4 V_A) around $t = 58.9$ min along L1 (L2). Notably, the direction of the peak ion flow at the magnetopause along L1 (yellow arrow) is nearly opposite to that along L2 (magenta arrow) in Figure 2a, as signatures of low-latitude magnetopause reconnection outflow. The local reconnection X-line as this time is identified by the magnetic separator—depicted as a thick gray curve in Figure 2a—with a high magnetic shear angle. This separator passes between L1 and L2 at the equator, further confirming the occurrence of reconnection. A detailed analysis of the magnetic separator and its role is provided in Section 3.1.2.

3.1.2. Global View on the Evolution of Dayside 3D X-Line and Related Reconnection

While evidence of reconnection at various latitudes along the magnetopause provides valuable insights into the global evolution of dayside reconnection, a more efficient and comprehensive analysis can be achieved by examining the magnetic field topology. In a two-dimensional context, magnetic reconnection typically occurs at an X-line. In 3D space, the analog of the 2D X-line is the 3D magnetic separator (Dorelli et al., 2007; Parnell et al., 2010; Priest & Forbes, 2000). On the dayside magnetosphere, magnetic field lines can be categorized into four distinct topological types. The first type is fully open with both ends extending into the solar wind. The second type is closed, connecting the southern and northern polar ionospheres. These two types are separated by the outer and inner separatrix surfaces (Pontin & Priest, 2022), with the dayside magnetopause located between them. At the contact point between the outer and inner separatrix surface—where the magnetic shear is sufficiently high—reconnection can occur, giving rise to two additional types of field lines: reconnected open field lines, which have one end connected to the solar wind and the other to either the Northern or Southern polar region. This classification implies that dayside reconnection necessarily occurs along the magnetic separator—the topological boundary where all four types of magnetic field lines converge.

Various methods have been developed to identify the magnetic separator in the dayside magnetosphere using three-dimensional magnetic field configurations from global simulations (e.g., Glocer et al., 2016; Komar et al., 2013). To efficiently approximate the path of the magnetic separator from a global perspective, we employ a direct field-line tracing method. A grid is first constructed in angular space, spanning [−90°, 90°] in both latitude and longitude, with 6° intervals. From each point on a radial line at the latitude-longitude grid intersections, magnetic field lines are traced to determine the outer separatrix as the boundary between fully open field lines and those with one of the other three topologies. The full 3D structure of the separator is then reconstructed by fitting the transition boundary between the two types of partially open field lines on the inner side of the separatrix surface using a continuous curve within the angular coordinate grid.

We determine the 3D location of the magnetic separator at each time frame, as sampled and shown in Figure 3. Figures 3a–3c correspond to stage 1–3, respectively. A distinct westward shift of the reconnection X-line is observed between stages 2 and 3 (Figures 3b and 3c). This shift is especially prominent at low latitudes, where the X-line shifts from the afternoon sector toward the noon sector of the magnetopause.

The magnetic shear angle between field lines just inside and outside the magnetic separator is represented by the color distribution along the magnetic separator in Figure 3. For any point $\boldsymbol{X}$ on the magnetic separator, two neighboring points are selected: $\boldsymbol{P} = \boldsymbol{X} - \mathrm{d}\,\boldsymbol{n_s}$ and $\boldsymbol{O} = \boldsymbol{X} + \mathrm{d}\,\boldsymbol{n_s}$, where $\boldsymbol{n_s}$ denotes the magnetopause normal direction, and d is set to $1\mathrm{R_E}$. The shear angle α is calculated as $\alpha = \arccos\left(\frac{\boldsymbol{B_P}\cdot\boldsymbol{B_O}}{|\boldsymbol{B_P}||\boldsymbol{B_O}|}\right)$, where $\boldsymbol{B_P}$ and $\boldsymbol{B_O}$ are the magnetic field vectors at points P and O, respectively. As shown in Figure 3, high-latitude X-points consistently exhibit large shear angle ($\alpha > 135°$), indicating anti-parallel field reconnection (Crooker, 1979). In contrast, the shear angle at low latitudes is initially too small ($\alpha < 45°$) to support reconnection during stages 1 and 2 but increases to a sufficiently level ($\alpha \sim 90°$) during stage 3, enabling low-latitude reconnection in accordance with the Maximum Magnetic Shear Model (Trattner et al., 2007, 2021). This evolution of the magnetic separator

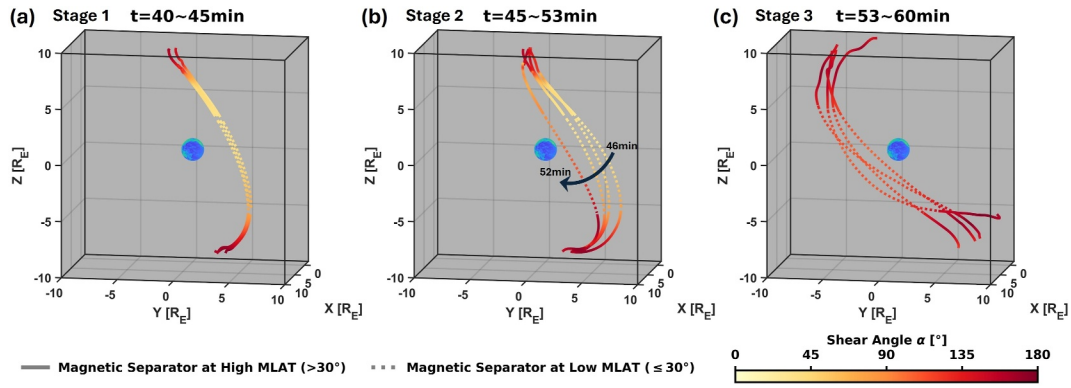

Figure 3. Evolution of magnetic separator at stage 1–3 in (a)–(c), separately. The time interval for the display is 2 min. The color represents the local shear angle. The shear angle on the magnetic separator at high latitudes (full lines) remains above 135° throughout, while at low latitudes (dashed lines), it changes from very small values (<45°) before 53 min to higher values (∼90°) thereafter.

suggests that while reconnection persists at the high-latitude dawn and dusk flanks of the magnetopause throughout the RD passage, driven by the consistently high IMF B_y/B_z ratio, low-latitude reconnection near noon is only triggered after the RD passes through the dayside magnetosheath, when the local B_z component of the magnetosheath field switches from positive to negative.

3.2. Ion Precipitation on the Northern Hemisphere Associated With Dayside Reconnection

The steady IMF conditions during stages 1 and 3 result in relatively steady ion precipitation, with a transition period occurring in stage 2. In this section, we examine ion precipitation in the northern polar region during stages 1 and 3 to assess its association with dayside magnetopause reconnection sites. We also compared the simulated precipitation with observational data to evaluate the model's consistency with real-world measurements.

3.2.1. Ion Precipitation Structures in Northern Polar Region

At the simulation's inner boundary surface at r = 3 R_E, ions within the loss cone that are able to precipitate along dipole magnetic field lines to r = 1 R_E—conserving both energy and magnetic moment—are identified as precipitating ions. Figures 4a and 4b show the distributions of the integrated energy flux of ion precipitation in the northern hemisphere at the inner boundary during t = 40–46 min and t = 54–60 min, corresponding to stages 1 and 3, respectively. The primary ion precipitation features appear as regions with enhanced integrated energy flux exceeding 100 eV.

Before the RD arrives in stage 1, two primary ion precipitation structures with high energy flux are evident: one located on the afternoon side in the open field line region, marked as point A (red) at (MLT, MLAT) = (13.3, 74.3°), and the other on the prenoon side in the closed field, marked as point B (blue) at (MLT, MLAT) = (9, 71.6°) (Figure 4a). This is not entirely consistent with the one-cusp-at-noon ion precipitation configuration reported Bobra et al. (2004) under similar negative IMF B_y conditions, where $|B_y|$–$|B_z|$, as possibly due to differences in the IMF B_x component or the tilt angle.

After the RD passes during stage 3, a broader precipitation region emerges, spanning from MLT 8 to 13. This region comprises three distinct yet connected substructures—an afternoon-side structure, a middle structure, and a prenoon-side structure—forming a longitudinally continuous band (Figure 4b).The afternoon and prenoon structures remain labeled as point A (red) at (MLT, MLAT) = (12.3, 74.3°) and point B (blue) at (MLT, MLAT) = (8, 73.4°), respectively. Compared to stage 1, points A and B exhibit minimal variation in integrated energy flux, latitudinal position, and magnetic topology, but both shift westward by approximately 15° in magnetic local time. This westward displacement is attributed to the enhancement in the IMF By component, which increases from −10 nT in stage 1 to −15 nT in stage 3, consistent with the observed IMF By-driven cusp motion (e.g., Escoubet et al., 2013) and the westward shift of high-latitude reconnection sites (see Figure 3b). Notably, a third precipitation structure, denoted as point C (green) at (MLT, MLAT) = (9.7, 72.5°), appears between points A and B in stage 3, exhibiting significantly stronger precipitation flux.

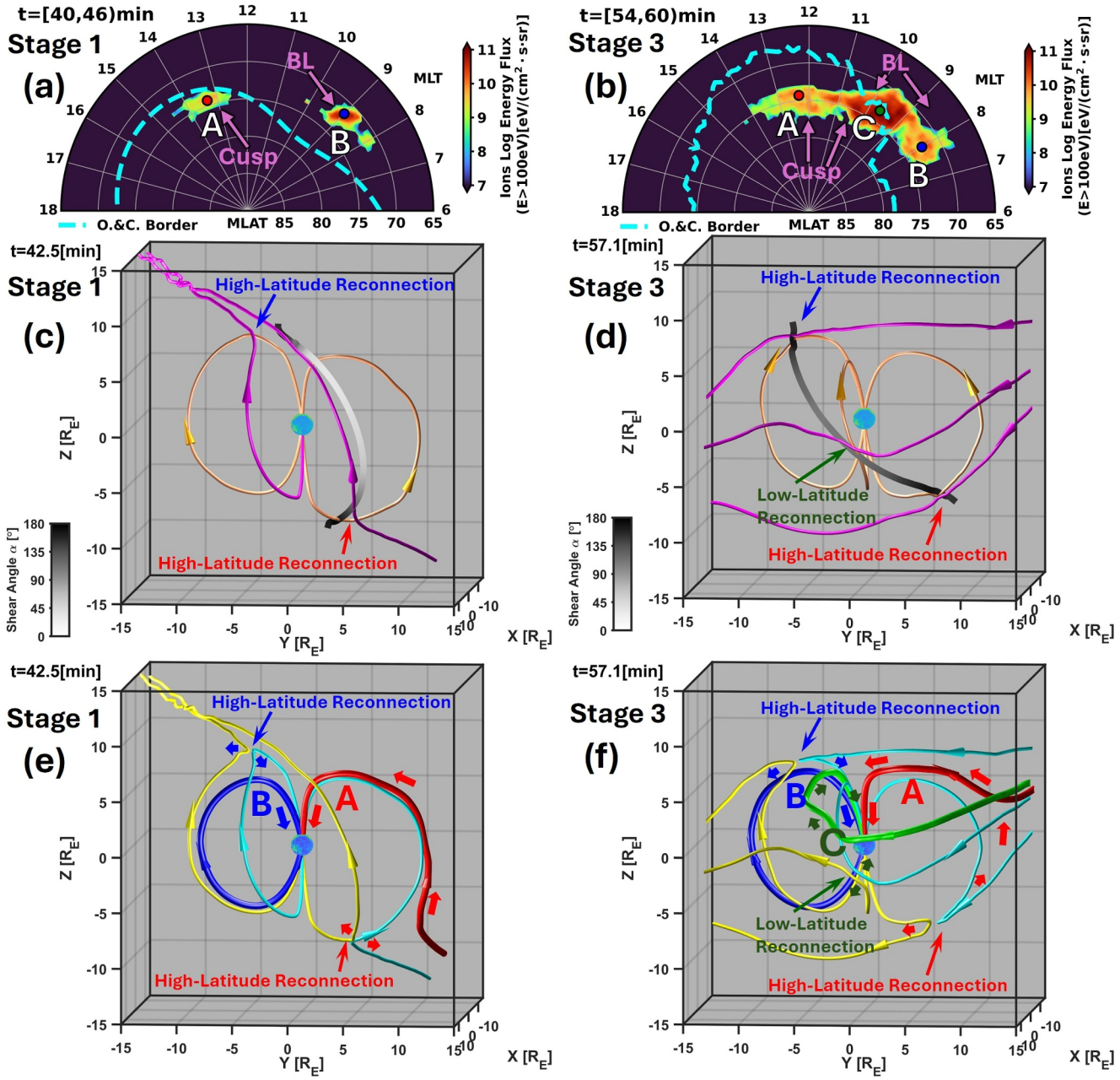

Figure 4. Cusp ion precipitation at the dayside northern hemisphere before rotational discontinuitie (RD) arrival (in stage rbs1) and after RD passage of dayside (in stage 3), with corresponding reconnection sites at the dayside. (a) Map of ion integrated energy flux distribution at the dayside northern hemisphere on the inner boundary in simulation for stage 1. Cusps and boundary layer (BL) are identified and marked by pink arrows. (b) The same as (a) but for stage 3. The Cyan dashed curve marks the open-closed boundary. Points A (red), B (blue), and C (green) are sampled points for each main ion precipitation structure. (c), (d) Dayside reconnection sites and inflow magnetic field lines (thin magenta and orange tubes). The magnetic separator is illustrated as a thick line with color representing the shear angle. (e), (f) Magnetic field lines connecting points A, B, and C (thick red, blue, and green tubes) in (a) or (b) and related outflow reconnected field lines (thin yellow and cyan tubes). Thick red, blue or green arrows indicate reconnection outflow and associated precipitation ion flow direction toward points A, B, or C representing each precipitation structure.

To aid in identifying these structures, the projected open–closed magnetic field boundary at each corresponding time is overlaid as a cyan dashed curve. Based on the magnetic topology, point A in stage 1 and point A along with the open-field portion of point C in stage 3 are associated with the cusp region, while the remaining parts—particularly in closed magnetic field regions—likely correspond to boundary layer ion precipitation (Song & Russell, 1992).

3.2.2. Multiple Sites of Reconnection Related With Multiple Ion Precipitation Structures

The time frames at $t = 42.5$ min (Figures 4c and 4e) and $t = 57.1$ min (Figures 4d and 4f) are selected to illustrate the steady dayside reconnection associated with the northern polar ion precipitation structures during stages 1 and 3, respectively. Magnetic reconnection sites are identified around the 3D magnetic separator with a high shear angle (thick line shades in grayscale in Figures 4c and 4d). Potential ion precipitation sources are located on the outflow side of these reconnection sites, where newly reconnected magnetic field lines (red, blue, and green thick tubes in Figures 4e and 4f) connect to specific points within the different polar precipitation structures (point A, B and C in Figures 4a and 4b).

The magnetic field lines before and after reconnection are illustrated by orange/magenta tubes in Figures 4c and 4d, and cyan/yellow tubes in Figures 4e and 4f, respectively. The thick red, blue, and green thick arrows denote the directions of the reconnection outflows and the subsequent motion of ions toward the northern polar region. In Figure 4c (stage 1, positive IMF B_z), the ion precipitation is associated with high-latitude reconnection sites in both the southern and northern hemispheres, corresponding to precipitation structures A and B (as shown in Figure 4e), consistent with the anti-parallel merging model (Crooker, 1979). Notably, in Figure 4c, one pre-reconnection field line (magenta) in the northern hemisphere is not fully open but connects to the southern polar region, indicating a re-reconnection event—where a previously reconnected field line and a closed magnetospheric field undergo a second reconnection. Similar second reconnections under northward IMF have also been reported in observations (Fuselier et al., 2012).

After the RD passes (Figures 4d and 4f, under negative IMF B_z), two high-latitude reconnection sites, again associated with structures A and B, are present, while a new low-latitude reconnection site emerges, associated with structure C. On the simulation's inner boundary in the northern hemisphere, the magnetic footpoints of field lines connected to the cusp are displaced westward by tens of degrees relative to their associated reconnection sites. This displacement is attributed to the westward $\mathbf{E} \times \mathbf{B}$ convection of the ions during their field-aligned motion.

In summary, during stage 1, ion outflows from high-latitude reconnection sites in both hemispheres give rise to the two main precipitation structures. In contrast, during stage 3, ion outflows from two high-latitude and one low-latitude reconnection sites result in the formation of three distinct yet connected precipitation structures in the dayside northern hemisphere.

3.2.3. Comparison of Ion Precipitation Structures in Observations and Simulations

The Defense Meteorological Satellite Program (DMSP) satellites have a nearly circular polar orbit at an altitude of approximately 835 km. The onboard SSJ instrument measures in situ ion precipitation across an energy range of 30 to 30 keV (Hardy, 1984). During the 10 April 2015 event, four DMSP satellites provided relevant observational data. The time intervals corresponding to stages 1–3 of the RD event are determined based on the simulation-derived timing relative to the RD's arrival at the Earth's bow shock nose (see Figure 1a). Prior to the RD's arrival (stage 1), DMSP F16 traversed the northern hemisphere between 05:58 and 06:08 UT. During the RD's transit through the dayside magnetosphere (stage 2), DMSP F18 passed through the dayside northern hemisphere between 06:10 and 06:16 UT, capturing precipitation features during this transitional period. Following the RD's passage (stage 3), DMSP F17 and F19 crossed the northern hemisphere cusp region at approximately 06:21 UT and 06:44 UT, respectively.

Ion precipitation observations from DMSP F16 and F17/F19 were selected for comparison with the simulated ion precipitation in the northern hemisphere during stages 1 and 3, respectively. Figure 5a–5c present the observed precipitating ion integrated energy flux (top panels) and the corresponding energy spectra of energy flux (bottom panels) along the orbit trajectories of DMSP F16 in stage 1, and DMSP F17/F19 in stage 3, respectively.

In the simulations, the approximate satellite trajectories are indicated by magenta lines on the integrated ion energy flux maps shown in Figures 5d–5f. These virtual trajectories do not perfectly align with the actual DMSP paths due to several simplifying assumptions in the simulation setup. Specifically, the simulations neglect dipole tilt, assume an idealized ionosphere, and use temporally averaged solar wind conditions rather than the perturbed values present on either side of the RD. Additionally, the simulation's inner boundary is set at $r = 3\ R_E$, which corresponds to an altitude of approximately 12,700 km, whereas the DMSP satellites operate at an altitude of roughly 835 km. These factors contribute to discrepancies in the angular positions of the ion precipitation

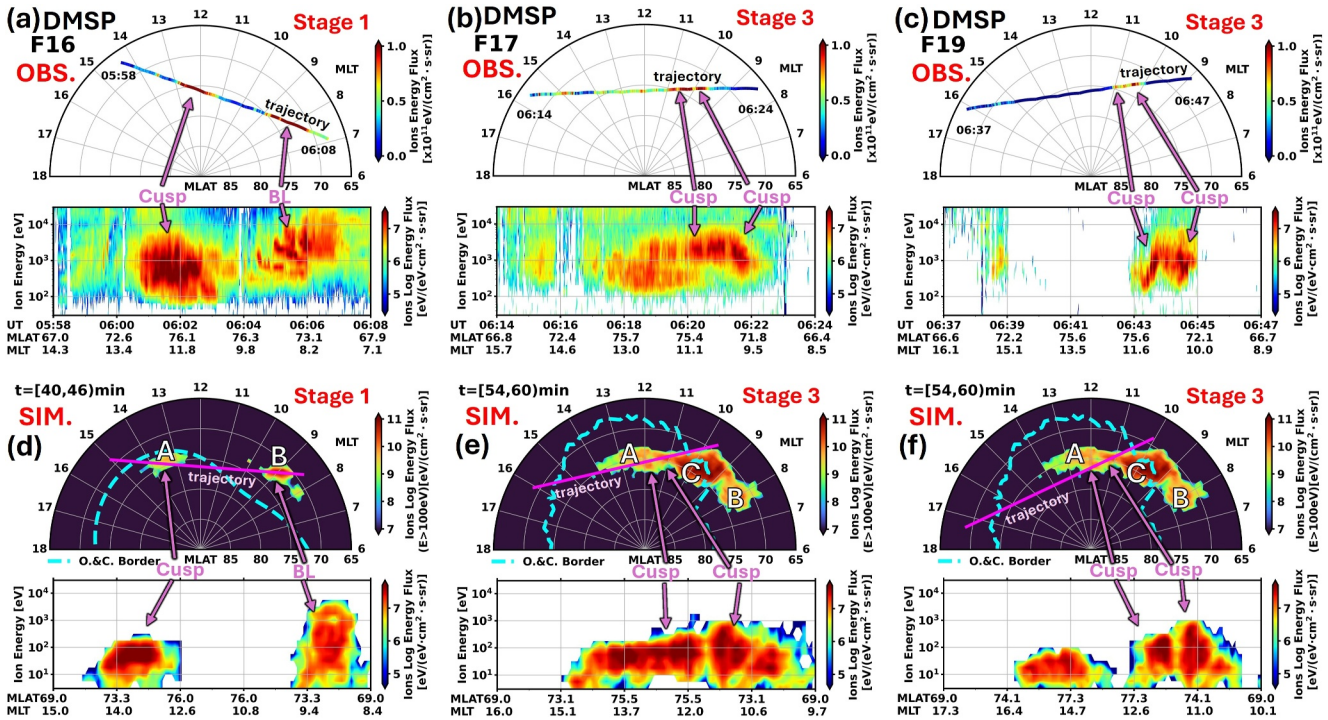

Figure 5. Comparison of ion precipitation on the dayside northern hemisphere in observations of the Defense Meteorological Satellite Program (DMSP) and global hybrid simulations. Cusps and boundary layer (BL) are identified and marked by pink arrows. (a) Precipitation ion integrated energy flux distribution along the path of DMSP F16 satellite in stage 1 at up panel. Bottom panel is the ions differential energy flux distribution with energy and time for DMSP F16 satellite at the same time range in stage 1. (b), (c) Similar to (a) but for DMSP F17/F19 satellite observation in stage 3. (d) Map of precipitation ions integrated energy flux on the inner boundary in simulation at stage 1 at upper panel, the same as Figure 4a. (e), (f) Similar to d but for stage 3, the same as Figure 4b. In (d)–(f), the purple line is the potential corresponding satellite orbit in simulations. Bottom panel in (d)–(f) is the ion differential energy flux distribution with energy and position on the purple line.

structures between simulations and observations. Moreover, the westward $\mathbf{E} \times \mathbf{B}$ convection of ions between the simulation's inner boundary and the DMSP orbit results in an apparent westward displacement of cusp precipitation structures in the observations. To account for this shift and better align the modeled and observed cusp locations, the DMSP trajectories were effectively rotated about 15° eastward in the simulation frame. This adjustment allows identification of the corresponding ion precipitation regions in the simulations that match the DMSP observations.

In stage 1, the DMSP F16 observations (Figure 5a) align well with the two ion precipitation structures (A and B in Figure 5d) produced by high-latitude reconnection at MLT ∼9 and ∼13.5 along the corresponding satellite trajectory in the simulation. As shown in the ion energy flux spectrum from the simulation (Figure 5d), both structures exhibit minimal energy-time dispersion, consistent with the DMSP F16 measurements. This is likely due to the $\mathbf{E} \times \mathbf{B}$ convection direction being nearly perpendicular to the satellite's path. The afternoon-side structure (A) lies on open field-lines and features ions with mean energies below 3 keV, characteristic of cusp precipitation. In contrast, the prenoon-side structure (B) is in a newly closed field-line region and displays relatively higher mean ion energies, a feature also evident in observations. Structure B exhibits typical boundary layer signatures (Song & Russell, 1992), comprising a mixture of a cooler, cusp-like magnetosheath component and a hotter magnetospheric component. This structure is formed by high-latitude reconnection at the dawnside northern-hemisphere magnetopause, as illustrated in Figure 4c.

In stage 3, DMSP F17 and F19 observed a “double cusps” structure with opposite energy dispersions at MLTs between 9 and 11. In the simulations (Figures 5e and 5f), the corresponding virtual satellite trajectories intersect the eastern portion of structure A and the western portion of structure C, both located on open magnetic field lines. This results in a simulated “double cusp” pattern that closely resembles the observed one, including the characteristic opposite dispersion signatures. This opposite dispersion may result from the precipitation ions in the

"double cusps," each originating from high- and low-latitude reconnection sites, following different $\mathbf{E} \times \mathbf{B}$ convection directions during precipitation.

4. Summary and Discussion

The 3D global hybrid simulation code ANGIE3D was applied to investigate the dayside magnetopause reconnection and cusp ion precipitation under solar wind conditions resembling those during an RD event on 10 April 2015. The main results are summarized below:

1. Dayside reconnection sites extend significantly from high to low latitudes due to the RD passing through the magnetopause. Before the RD touches the bow shock, high-latitude reconnection remains steady near the dawn (dusk) side in the northern (southern) hemisphere under an upstream IMF of (10, −10, 10) nT. As the RD propagates into the magnetosheath, these high-latitude reconnection sites shift westward. After the RD passes through the dayside magnetopause, reconnection occurs simultaneously at both high and low latitudes under an IMF of (−7, −15, −5.1) nT. These results are well consistent with empirical dayside reconnection X-line models (Trattner et al., 2007, 2017, 2021).
2. The dayside polar ion precipitation structure evolves in response to the shifting reconnection sites associated with the RD. Before the RD interacts with the bow shock, two distinct ion precipitation structures are found in the northern hemisphere, resulting from simultaneous high-latitude reconnection in both hemispheres. After the RD passes through the dayside magnetopause, a longitudinal chain of three ion precipitation structures—from prenoon to noon—is observed in the northern polar region. These three structures account for steady dayside reconnection at northern high latitudes, low latitudes near noon, and southern high latitudes, respectively. Field line tracing and energy spectra analysis indicate that two of those three regions are located with the cusp, suggesting that simultaneous high- and low-latitude reconnection on the dayside magnetopause can produce the observed "double cusp" precipitation, consistent with the mechanism proposed by Wing et al. (2001).
3. The simulation results indicate that a possible new source at southern (northern) hemisphere high-latitude reconnection sites accounts for northern (southern) cusp ion precipitation under a high IMF B_y/B_z ratio. In the observational study by Wing et al. (2001), the "double cusp" structure was interpreted as resulting from low-low- and high-latitude reconnection within the same hemisphere, with the latter consistent with the anti-parallel merging model (Crooker, 1979). Our simulation also reproduces a "double cusp" pattern—structures A and C in Figure 4b. While cusp C is indeed connected to low-latitude reconnection, cusp A is found to be magnetically connected to a high-latitude reconnection site in the opposite hemisphere. This interhemispheric precipitation pathway aligns with the non-lobe reconnection mechanism proposed by Cowley (1983) and is supported by observations of parallel streaming magnetosheath ions flowing into the ionosphere in the opposite hemisphere, as discussed in Fuselier et al. (2018).

This study demonstrates the significant influence of a high IMF B_y/B_z ratio on magnetopause reconnection and ion precipitation. Under a positive B_z-dominant IMF, reconnection poleward of the cusp typically leads to cusp aurora near noon (e.g., Bobra et al., 2004). In our simulation, under a higher B_y/B_z ratio when $B_z > 0$, the high-latitude reconnection sites shift toward the dawn or dusk flanks on the dayside, resulting in a shift of cusp precipitation toward the afternoon sector in the northern hemisphere. Conversely, under negative B_z-dominated IMF, dayside reconnection is typically confined near the equator, producing the classic latitudinally dispersed of cusp ion signatures (e.g., Frey, Phan, et al., 2003, Frey, Mende, et al., 2003). In our simulation with a high B_y/B_z ratio when $B_z < 0$, high-energy precipitation ions from both high-and low-latitude reconnection sites occur at comparable latitudes, deviating from the conventional expectation that ions from higher-latitude reconnection should precipitate at higher magnetic latitudes. The ion energy spectra (see Figure 5) from both simulations and DMSP observations reveal dispersions not only in latitude but also in longitude, suggesting a more complex ion transport and precipitation pattern under high IMF B_y/B_z conditions. These results highlight the need for further investigation using advanced 3D simulations to fully understand the ionospheric signatures of such reconnection geometries.

The comparison between simulations and observations in this study offers valuable insights for analyzing in situ satellite measurements of precipitation ion properties. The statistical investigation of cusp occurrences on either side of noon, as conducted by Newell et al. (1995, 2004), revealed that cusp occurrences tend to skew toward prenoon when IMF $B_y < 0$ and toward postnoon when IMF $B_y > 0$. This finding aligns with the expected anti-

parallel reconnection at high latitudes within the same hemisphere. However, based on the simulation results presented here, we suggest considering an alternative possibility: that cusp ions observed at postnoon (prenoon) when IMF $B_y < 0$ (IMF $B_y > 0$) may originate from high-latitude reconnection occurring in the opposite hemisphere, particularly under conditions of IMF Bz > 0. This hypothesis warrants further observational investigation to better understand cusp dynamics and reconnection asymmetries.

Our study demonstrates the reliability of 3D global hybrid-PIC simulations (e.g., Tan et al., 2012) as an effective tool for investigating the physical processes underlying the ion precipitation under various solar wind conditions. The simulated polar ion precipitation structures exhibit relative positions and spatial dispersions that are consistent with satellite observations during the corresponding RD event, validating the model's capability to reproduce key features of dayside magnetospheric dynamics.

Data Availability Statement

The Air Force Research Laboratory and the World Data Center provided the DMSP SSJ4/SSJ5 data. The DMSP data are available online at http://sd-www.jhuapl.edu/Aurora/spectrogram/. NASA OMNIweb (https://omniweb.gsfc.nasa.gov/) provides the 1-min resolution solar wind data. The simulation data are available at Li and Xueyi (2025).

Acknowledgments
This work at Auburn University is supported by NASA Grants 80NSSC23K0896, 80NSSC23K0086, 80NSSC22K1012, and the NSF Grants AGS-2131012, AGS-2247759, and AGS-2224109. Computer resources were provided by NASA Advanced Supercomputing (NAS) Division. Simon Wing acknowledges the support of NASA Grants 80NSSC22K0515, 80NSSC23K0904, 80NSS23K0899, and NSF GEO/AGS Grant 2431665. C.-P. Wang is supported by NASA 80NSSC22K1012 and NSF-GEM 2224108.

References

Andréeová, K., & Přech, L. (2007). Propagation of interplanetary shocks into the Earth's magnetosphere. *Advances in Space Research*, *40*(12), 1871–1880. https://doi.org/10.1016/j.asr.2007.04.079

Bobra, M. G., Petrinec, S. M., Fuselier, S. A., Claflin, E. S., & Spence, H. E. (2004). On the solar wind control of cusp aurora during northward IMF. *Geophysical research letters*, *31*(4), L04805. https://doi.org/10.1029/2003gl018417

Borovsky, J. E., & Denton, M. H. (2006). Differences between CME-driven storms and CIR-driven storms. *Journal of Geophysical Research*, *111*(A7), A07S08. https://doi.org/10.1029/2005ja011447

Burlaga, L. F. (1969). Directional discontinuities in the interplanetary magnetic field. *Solar Physics*, *7*(1), 54–71. https://doi.org/10.1007/bf00148406

Connor, H. J., Raeder, J., & Trattner, K. J. (2012). Dynamic modeling of cusp ion structures. *Journal of Geophysical Research*, *117*(A4), A04203. https://doi.org/10.1029/2011ja017203

Connor, H. K., Raeder, J., Sibeck, D. G., & Trattner, K. J. (2015). Relation between cusp ion structures and dayside reconnection for four IMF clock angles: OpenGGCM-LTPT results. *Journal of Geophysical Research: Space Physics*, *120*(6), 4890–4906. https://doi.org/10.1002/2015ja021156

Cowley, S. W. (1983). Interpretation of observed relations between solar wind characteristics and effects at ionospheric altitudes. In *High-latitude space plasma physics* (pp. 225–249). Springer US.

Cowley, S. W. H., & Owen, C. J. (1989). A simple illustrative model of open flux tube motion over the dayside magnetopause. *Planetary and Space Science*, *37*(11), 1461–1475. https://doi.org/10.1016/0032-0633(89)90116-5

Crooker, N. U. (1979). Dayside merging and cusp geometry. *Journal of Geophysical Research*, *84*(A3), 951–959. https://doi.org/10.1029/ja084ia03p00951

Dorelli, J. C., Bhattacharjee, A., & Raeder, J. (2007). Separator reconnection at Earth's dayside magnetopause under generic northward interplanetary magnetic field conditions. *Journal of Geophysical Research*, *112*(A2), A02202. https://doi.org/10.1029/2006ja011877

Escoubet, C. P., Berchem, J., Trattner, K. J., Pitout, F., Richard, R., Taylor, M. G. G. T., et al. (2013). Double cusp encounter by cluster: Double cusp or motion of the cusp? In *Annales Geophysicae* Vol. 31(4), (pp. 713–723). https://doi.org/10.5194/angeo-31-713-2013

Farrugia, C. J., Lugaz, N., Wing, S., Wilson III, L. B., Sibeck, D. J., Cowley, S. W. H., et al. (2022). Effects from dayside magnetosphere to distant tail unleashed by a bifurcated, non-reconnecting interplanetary current sheet. *Frontiers in Physics*, *10*, 942486. https://doi.org/10.3389/fphy.2022.942486

Frey, H. U. (2007). Localized aurora beyond the auroral oval. *Reviews of Geophysics*, *45*(1), RG1003. https://doi.org/10.1029/2005rg000174

Frey, H. U., Mende, S. B., Fuselier, S. A., Immel, T. J., & Østgaard, N. (2003). Proton aurora in the cusp during southward IMF. *Journal of Geophysical Research*, *108*(A7), 1277. https://doi.org/10.1029/2003ja009861

Frey, H. U., Phan, T. D., Fuselier, S. A., & Mende, S. B. (2003). Continuous magnetic reconnection at Earth's magnetopause. *Nature*, *426*(6966), 533–537. https://doi.org/10.1038/nature02084

Fuselier, S. A., Mende, S. B., Moore, T. E., Frey, H. U., Petrinec, S. M., Claflin, E. S., & Collier, M. R. (2003). Cusp dynamics and ionospheric outflow. Magnetospheric imaging—the image prime mission (pp. 285–312).

Fuselier, S. A., Trattner, K. J., Petrinec, S. M., & Lavraud, B. (2012). Dayside magnetic topology at the Earth's magnetopause for northward IMF. *Journal of Geophysical Research*, *117*(A8), A08235. https://doi.org/10.1029/2012ja017852

Fuselier, S. A., Trattner, K. J., Petrinec, S. M., Lavraud, B., & Mukherjee, J. (2018). Nonlobe reconnection at the Earth's magnetopause for northward IMF. *Journal of Geophysical Research: Space Physics*, *123*(10), 8275–8291. https://doi.org/10.1029/2018ja025435

Fuselier, S. A., Trattner, K. J., Petrinec, S. M., Pritchard, K. R., Burch, J. L., Cassak, P. A., et al. (2019). Stationarity of the reconnection X-line at Earth's magnetopause for southward IMF. *Journal of Geophysical Research: Space Physics*, *124*(11), 8524–8534. https://doi.org/10.1029/2019ja027143

Glocer, A., Dorelli, J., Toth, G., Komar, C. M., & Cassak, P. A. (2016). Separator reconnection at the magnetopause for predominantly northward and southward IMF: Techniques and results. *Journal of Geophysical Research: Space Physics*, *121*(1), 140–156. https://doi.org/10.1002/2015ja021417

Grandin, M., Luttikhuis, T., Battarbee, M., Cozzani, G., Zhou, H., Turc, L., et al. (2023). First 3D hybrid-Vlasov global simulation of auroral proton precipitation and comparison with satellite observations. *Journal of Space Weather and Space Climate*, *13*, 20. https://doi.org/10.1051/swsc/2023017

Guo, Z., Lin, Y., & Wang, X. (2021). Global hybrid simulations of interaction between interplanetary rotational discontinuity and bow shock/magnetosphere: Can ion-scale magnetic reconnection be driven by rotational discontinuity downstream of quasi-parallel shock? *Journal of Geophysical Research: Space Physics*, *126*(4), e2020JA028853. https://doi.org/10.1029/2020ja028853

Guo, Z., Lin, Y., Wang, X., & Du, A. (2018). Magnetosheath reconnection before magnetopause reconnection driven by interplanetary tangential discontinuity: A three-dimensional global hybrid simulation with oblique interplanetary magnetic field. *Journal of Geophysical Research: Space Physics*, *123*(11), 9169–9186. https://doi.org/10.1029/2018ja025679

Guo, Z., Lin, Y., Wang, X., & Du, A. (2021). Magnetic reconnection inside solar wind rotational discontinuity during its interaction with the quasi-perpendicular bow shock and magnetosheath. *Journal of Geophysical Research: Space Physics*, *126*(12), e2021JA029979. https://doi.org/10.1029/2021ja029979

Hardy, D. A. (1984). Precipitating electron and ion detectors (SSJ/4) for the block 5D/flights 6-10 DMSP satellites: Calibration and data presentation. AFGL-TR-84-0317.

Hsu, T. S., & McPherron, R. L. (2003). Occurrence frequencies of IMF triggered and nontriggered substorms. *Journal of Geophysical Research*, *108*(A7), 1307. https://doi.org/10.1029/2002ja009442

Komar, C. M., Cassak, P. A., Dorelli, J. C., Glocer, A., & Kuznetsova, M. M. (2013). Tracing magnetic separators and their dependence on IMF clock angle in global magnetospheric simulations. *Journal of Geophysical Research: Space Physics*, *118*(8), 4998–5007. https://doi.org/10.1002/jgra.50479

Lavraud, B., & Cargill, P. J. (2005). Cluster reveals the magnetospheric cusps. *Astronomy and Geophysics*, *46*(1), 1.32–1.35. https://doi.org/10.1046/j.1468-4004.2003.46132.x

Lepping, R. P., & Behannon, K. W. (1986). Magnetic field directional discontinuities: Characteristics between 0.46 and 1.0 AU. *Journal of Geophysical Research*, *91*(A8), 8725–8741. https://doi.org/10.1029/ja091ia08p08725

Li, X., & Xueyi, W. (2025). Polar ion precipitation data in ANGIE3D simulation case of magnetosphere in response to solar wind rotational discontinuity (RD) as observed in April 9-11, 2015 [Dataset]. *Zenodo*. https://doi.org/10.5281/zenodo.14736218

Lin, Y., Wang, X. Y., Lu, S., Perez, J. D., & Lu, Q. (2014). Investigation of storm time magnetotail and ion injection using three-dimensional global hybrid simulation. *Journal of Geophysical Research: Space Physics*, *119*(9), 7413–7432. https://doi.org/10.1002/2014ja020005

Liou, K., Sotirelis, T., & Richardson, I. (2018). Substorm occurrence and intensity associated with three types of solar wind structure. *Journal of Geophysical Research: Space Physics*, *123*(1), 485–496. https://doi.org/10.1002/2017ja024451

Lukin, A., Guo, Z., Lin, Y., Panov, E., Artemyev, A., Zhang, X., & Petrukovich, A. (2024). Triggering the magnetopause reconnection by solar wind discontinuities. *The Astrophysical Journal*, *963*(2), 145. https://doi.org/10.3847/1538-4357/ad1e63

Newell, P. T., & Meng, C. I. (1994). Ionospheric projections of magnetospheric regions under low and high solar wind pressure conditions. *Journal of Geophysical Research*, *99*(A1), 273–286. https://doi.org/10.1029/93ja02273

Newell, P. T., Meng, C.-I., Sibeck, D. G., & Lepping, R. (1989). Some low-altitude cusp dependencies on the interplanetary magnetic field. *Journal of Geophysical Research*, *94*(A7), 8921–8927. https://doi.org/10.1029/JA094iA07p08921

Newell, P. T., Ruohoniemi, J. M., & Meng, C.-I. (2004). Maps of precipitation by source region, binned by IMF, with inertial convection streamlines. *Journal of Geophysical Research*, *109*(A10), A10206. https://doi.org/10.1029/2004JA010499

Newell, P. T., Sibeck, D. G., & Meng, C.-I. (1995). Penetration of the interplanetary magnetic field, b_y and magnetosheath plasma into the magnetosphere: Implications for the predominant magnetopause merging site. *Journal of Geophysical Research*, *100*(A1), 235–243. https://doi.org/10.1029/94JA02632

Parnell, C. E., Haynes, A. L., & Galsgaard, K. (2010). Structure of magnetic separators and separator reconnection. *Journal of Geophysical Research*, *115*(A2), A02102. https://doi.org/10.1029/2009ja014557

Petrinec, S. M., & Fuselier, S. A. (2003). On continuous versus discontinuous neutral lines at the dayside magnetopause for southward interplanetary magnetic field. *Geophysical Research Letters*, *30*(10), 1519. https://doi.org/10.1029/2002gl016565

Phan, T., Frey, H. U., Frey, S., Peticolas, L., Fuselier, S., Carlson, C., et al. (2003). Simultaneous Cluster and IMAGE observations of cusp reconnection and auroral proton spot for northward IMF. *Geophysical Research Letters*, *30*(10), 1509. https://doi.org/10.1029/2003gl016885

Pitout, F., Escoubet, C. P., Klecker, B., & Dandouras, I. (2009). Cluster survey of the middle altitude cusp: 2. Large-scale morphology. *Annals of Geophysics*, *27*(5), 1875–1886. https://doi.org/10.5194/angeo-27-1875-2009

Pontin, D. I., & Priest, E. R. (2022). Magnetic reconnection: MHD theory and modelling. *Living Reviews in Solar Physics*, *19*(1), 1. https://doi.org/10.1007/s41116-022-00032-9

Priest, E. R., & Forbes, T. G. (2000). *Magnetic reconnection: MHD theory and applications*. Cambridge Univ. Press.

Song, P., & Russell, C. T. (1992). Model of the formation of the low-latitude boundary layer for strongly northward interplanetary magnetic field. *Journal of Geophysical Research*, *97*(A2), 1411–1420. https://doi.org/10.1029/91ja02377

Tan, B., Lin, Y., Perez, J. D., & Wang, X. Y. (2011). Global-scale hybrid simulation of dayside magnetic reconnection under southward IMF: Structure and evolution of reconnection. *Journal of Geophysical Research*, *116*(A2), A02206. https://doi.org/10.1029/2010ja015580

Tan, B., Lin, Y., Perez, J. D., & Wang, X. Y. (2012). Global-scale hybrid simulation of cusp precipitating ions associated with magnetopause reconnection under southward IMF. *Journal of Geophysical Research*, *117*(A3), A03217. https://doi.org/10.1029/2011ja016871

Trattner, K. J., Mulcock, J. S., Petrinec, S. M., & Fuselier, S. A. (2007). Location of the reconnection line at the magnetopause during southward IMF conditions. *Geophysical Research Letters*, *34*(3), L03108. https://doi.org/10.1029/2006gl028397

Trattner, K. J., Petrinec, S. M., & Fuselier, S. A. (2021). The location of magnetic reconnection at Earth's magnetopause. *Space Science Reviews*, *217*(3), 41. https://doi.org/10.1007/s11214-021-00817-8

Trattner, K. J., Thresher, S., Trenchi, L., Fuselier, S. A., Petrinec, S. M., Peterson, W. K., & Marcucci, M. F. (2017). On the occurrence of magnetic reconnection equatorward of the cusps at the Earth's magnetopause during northward IMF conditions. *Journal of Geophysical Research: Space Physics*, *122*(1), 605–617. https://doi.org/10.1002/2016ja023398

Wang, H., Lin, Y., Wang, X., & Guo, Z. (2019). Generation of kinetic Alfvén waves in dayside magnetopause reconnection: A 3-D global-scale hybrid simulation. *Physics of Plasmas*, *26*(7), 072102. https://doi.org/10.1063/1.5092561

Wing, S., Berchem, J., Escoubet, C. P., & Farrugia, C. (2024). Complex dayside particle precipitation observed during the passage of a solar wind rotational discontinuity. *Frontiers in Astronomy and Space Sciences*, *11*, 1320809. https://doi.org/10.3389/fspas.2024.1320809

Wing, S., Berchem, J., Escoubet, C. P., Farrugia, C., & Lugaz, N. (2023). Multispacecraft observations of the simultaneous occurrence of magnetic reconnection at high and low latitudes during the passage of a solar wind rotational discontinuity embedded in the April 9-11, 2015 ICME. *Geophysical Research Letters*, *50*(9), e2023GL103194. https://doi.org/10.1029/2023gl103194

Wing, S., Newell, P. T., & Onsager, T. G. (1996). Modeling the entry of magnetosheath electrons into the dayside ionosphere. *Journal of Geophysical Research*, *101*(A6), 13155–13167. https://doi.org/10.1029/96JA00395

Wing, S., Newell, P. T., & Ruohoniemi, J. M. (2001). Double cusp: Model prediction and observational verification. *Journal of Geophysical Research*, *106*(A11), 25571–25593. https://doi.org/10.1029/2000ja000402

Yermolaev, Y. I., Nikolaeva, N. S., Lodkina, I. G., & Yermolaev, M. Y. (2012). Geoeffectiveness and efficiency of CIR, sheath, and ICME in generation of magnetic storms. *Journal of Geophysical Research*, *117*(A9), A00L07. https://doi.org/10.1029/2011ja017139

Zong, Q.-G., Zong, Q.-G., Zhang, H., Fritz, T. A., Goldstein, M., Wing, S., et al. (2008). Multiple cusps during an extended northward IMF period with a significant by component. *Journal of Geophysical Research*, *113*, A01210. https://doi.org/10.1029/2006JA012188